Energy Transfer in Mixed Lanthanides Complexes: Towards High-Performance Pressure Sensors Based on the Luminescence Intensity Ratio

Yujiao Zhou, Gilles Ledoux, Laurence BOIS, Guillaume Pilet, Margherita Colombo, Erwann Jeanneau, Lionel Lafarge, Catherine Journet, Sylvie Descartes, David Philippon

Energy Transfer in Mixed Lanthanides Complexes: Towards High-Performance Pressure Sensors Based on the Luminescence Intensity Ratio

Yujiao ZHOU[1,2], Gilles LEDOUX[3], Laurence BOIS[1]*, Guillaume PILET[1], Margherita COLOMBO[1], Erwann JEANNEAU[4], Lionel LAFARGE[2], Catherine JOURNET[1], Sylvie DESCARTES[2], David PHILIPPON[2]*

[1] Laboratoire des Multimatériaux et Interfaces, UMR CNRS 5615, 6, rue Victor Grignard, Université Lyon1-CNRS, 69622 Villeurbanne Cedex, France

[2] Univ Lyon, INSA Lyon, CNRS, LaMCoS - UMR5259, 27 bis Av. Jean Capelle, 69621 Villeurbanne, France

[3] Institut Lumière Matière, UMR CNRS 5306, 10 Rue Ada Byron, Université Lyon1-CNRS, 69622 Villeurbanne Cedex, France

[4] Centre de Diffractométrie Henri Longchambon, Université Lyon1-CNRS, 69622 Villeurbanne Cedex, France

Keywords: Lanthanide complexes, luminescence, pressure sensor, energy transfer

Abstract:

In this study, we present a reversible pressure-sensing material with high sensitivity. Mixed β-diketonate complexes of Tb^{3+} and Eu^{3+} [(Ln)$(acac)_3$phen] are synthesized with phenanthroline as an ancillary ligand. The organic ligands provide the antenna effect to make the Ln^{3+} complex excitable at 405 nm. Eu^{3+} emission results from efficient energy transfer (ET) from Tb^{3+}. Under 405 nm excitation, the emission intensity of Tb^{3+} decreases whereas the emission intensity of Eu^{3+} increases with pressure, making this complex a potential pressure sensor based on luminescent-intensity-ratio (LIR) up to 700 MPa. This study then discusses the application of this Tb^{3+}/Eu^{3+} complex for pressure sensing depending on measurement conditions. The addition of the optically neutral ion Y^{3+} to the system can reduce the impact of pressure-induced structural defects on the emission, thus improving the reversibility of the LIR variation as a function of pressure. Therefore, a self-calibrating, reliable, and reversible pressure-sensing material is proposed here, with remarkable pressure sensitivity compared to a peak shift-based pressure sensor.

1 Introduction

In recent decades, photoluminescent sensors have received increasing attention in various applications.[1–4] When light is used as an information carrier for a measurement device or sensor, advantages such as noncontact, high penetrability, and fast response allow substantial temporal and spatial resolution. Depending on the physicochemical characteristics of the materials, their photoluminescence can be sensitive to various physical variables. Among various photoluminescent (PL) sensors, [5,6,15–22,7–14] those related to pressure sensing are a hot topic in many fields of basic science, technology and engineering, such as biology,[23] tribology, [24,25] and optics.[26] Rare-earth based compounds are among the most interesting and reliable materials to develop thanks to their long emission lifetime, sharp emission peak, low toxicity, and high functionalizability.

In a photo-radiation system, as the dipole strength of 4f-4f transitions of Ln^{3+} ions is considerably low, direct excitation of the 4f levels requires a wavelength-specific energy source with considerable excitation power. Therefore, the sensitization of Ln^{3+} through other means, such as a good light absorber, has been studied and is known as the '*Antenna effect*'.[27] The energy donor is often an organic ligand.[28–35] In an organic complex, the antenna effect can be very effective due to the strong interaction between the ligand and the metal.[27,28,32,36–39] The singlet excited state S_1 of the ligand can be deactivated by a non-relaxation process (NR) or intersystem crossing (IC) to the triplet T_1, and energy transfer (ET) continues from T_1 to the Ln^{3+} emissive level. Although the interaction between the ligand and the metal in a lanthanide organic complex is typically observed, energy transfer between the ligand and the metal (L-M and M-L ET) is not the only pathway. Structural imperfections in a solid system can lead to notable non-radiative relaxation, reducing or even canceling light emission. This phenomenon is usually observed in systems with a high concentration of Ln^{3+}, where energy migration can occur (also known as concentration quenching).[34,40] The main mechanism is determined by the relative rate constant of the different processes involved. For example, M-M ET can easily occur when the interionic distance is sufficiently close.[41–45] Such ET can only occur if there is a spectral overlap between the emission of the sensitizer (donor) and the absorption of the emitter (acceptor). The theory of Förster resonance ET (FRET) was first proposed by Theodor Förster in 1946 to determine the rate of ET between two dipoles.[41] When two Ln^{3+} are close enough to reach their critical distance (R_0), the probability of energy transfer (ET) and spontaneous deactivation of the ion donor starts to equalize. The R_0 can be as large as 10 Å in a dipole-dipole (metal-metal) FRET system, whereas the dipole-quadrupolar mechanism (ligand-metal) may need to reach 3 Å to equalize the ET efficiency.[34] In a dipole-dipole FRET system, the distance dependence of the ET rate is given by R^6, resulting in a high sensitivity to crystal lattice contraction or distortion under increased pressure. To date, this methodology has been mainly applied to ET between Ln^{3+}-Ln^{3+} in an inorganic host as high-pressure-sensitive phosphors for various applications.[23,46] For example, Yb^{3+} and Tm^{3+} doped $LaPO_4$, and YPO_4 upconversion nanoparticles were developed as pressure sensors by Runowski *et al.*[17] The change in ET from Yb^{3+} to Tm^{3+} caused by many effects such as the decrease in Yb^{3+}-Tm^{3+} distance with applied pressure, the increased multiphonon-relaxation, the improved covalency and increased crystal field strength,[47–50] results in the relative intensity ($^3H_4$ -> $^3H_6$/$^1G_4$ -> $^3H_6$), lifetime, peak position and FVHM of the Tm^{3+} peak varying with pressure up to 26 GPa. In a lower pressure range (≤10 GPa), the pressure-sensing properties of Yb^{3+}/Er^{3+} doped upconversion nanoparticles have shown a red/green ratio, a lifetime and brightness of Er^{3+} varying with pressure.[18,51] Furthermore, the pressure sensitivity of SrF_3: Yb^{3+}, Er^{3+} have been reported by Runowski's, with variations in lifetime, emission intensity, and peak centroid observed under compression ≤5.5 GPa.[12] Recent works have allowed increasing sensitivity to 9 nm/GPa in Eu^{2+}:$Sr_8Si_4O_{12}Cl_8$ [47] and even to 23 nm/GPa in Cr^{3+}:$LiScGeO_4$[52]. Moreover, with mechanoluminescent materials such as ZnS/CaZnOS:Mn^{2+}, a very high sensitivity up to 6.2 nm/GPa has been achieved.[53] In the low-range pressure, pressure-sensibility induced by the vacuum-enhanced light-to-heat conversion effect has also been demonstrated.[20,50,54] However, the utilization of lanthanide complexes for optical pressure sensing has been relatively unexplored thus far.

Several studies on Ln complexes sensitive to high hydrostatic pressure have been reported based on the ET between Ln^{3+} and the organic ligand.[55–57] Wong *et al.* showed hydrostatic compression (<6 GPa) leads to a decrease in the emission intensity of the Eu^{3+} β-diketonate complex because the shorter distances of the Ln^{3+}-ligand and ligand-ligand increase the probability of nonradiative

relaxation.[56] Furthermore, pressure sensitivity under 140 kPa is well documented and related to oxygen-sensitivity.[58,59] However, the evolution of photoluminescence under pressure in a complex based on Ln^{3+}-Ln^{3+} ET has not been developed to the best of our knowledge.

In this study, we have investigated the pressure sensitivity of a mixed Tb^{3+} and Eu^{3+} β-diketonate complex with phenanthroline as an ancillary ligand. Building upon previous research on Tb^{3+} and Eu^{3+} β-diketonate complexes,[60–62] we developed [(Ln)(acac)$_3$phen] complexes, where acac = acetylacetonate and phen = 1,10-phenanthroline. The addition of the [phen] ligand to the structure is designed to enhance the antenna effect and increase the intensity of photoluminescent emission.[32,63,72,64–71] This property has been used in electroluminescence since 1996.[73–75] More importantly, Tb^{3+} is a well-known sensitizer of Eu^{3+} due to the close energy level match ($^5D_4 \rightarrow {}^7F_5$ = $^7F_1 \rightarrow {}^5D_1$).[4,5,65,76–80] Furthermore, since the emission peaks of Tb^{3+} and Eu^{3+} are generally distinct, it is possible to analyze their emissions separately. Moreover, compared to a purely inorganic host, the organic ligand provides more structural flexibility,[81] facilitating structural changes under moderate pressure. Our intention is to utilize the Tb^{3+}/Eu^{3+} β-diketonate complex as a highly sensitive pressure sensor in the pressure range of 0-1 GPa. Capitalizing on the distinct emission peaks of Tb^{3+} and Eu^{3+}, we aim to use changes in the luminescent intensity ratio (LIR) to track changes in pressure. This method, which is independent of emission intensity and peak position, can be considered 'self-calibrated.' Using the excitation of an organic ligand, the Tb^{3+}-Eu^{3+} ET in the complex was studied as a function of various parameters, including Ln^{3+} concentration, dilution with Y^{3+} ions, temperature, and applied pressure.

2 Results and discussion

Here, we first present the structural characterization of the complex. Then, the optical analysis section will be divided into three parts: a) excitation and emission spectra at room temperature (298 K) and at low temperatures (93 K); b) lifetime measurements of the complex at different compositions under two atmospheres (in air and in N_2) for O_2 quenching control; and c) lifetime measurements at different temperatures.

2.1 Crystal structure analysis

The prepared dry crystal is an opaque white, needle-shaped solid. After soft grinding, the powder was analyzed by X-ray diffraction. Figures 1a and S1 show the X-ray diffraction patterns of the complex in different compositions. The structure is similar to the reference (CCDC 1482080[67,82]): $C_{27}H_{29}N_2O_6Ln$ (Ln^{3+}= Tb^{3+}, Eu^{3+}), corresponding to one Ln, three [acac] ligands and one [phen] ligand per molecule. The slight difference in the peak around 12° can be explained by the polymorphism in the [phen] coordinated complex.[83] Structural resolution of the [$Eu_{0.01}Tb_{0.20}Y_{0.79}$(acac)$_3$phen] complex on a single crystal was conducted and confirms that it has the same structure as the monometallic Tb or Eu complexes.[84] The [$Eu_{0.01}Tb_{0.20}Y_{0.79}$(acac)$_3$phen] compound is a mononuclear complex in which the Ln^{3+} ion is coordinated by three deprotonated acac-ligands and one neutral phenanthroline. Its refined formula is therefore [Ln(acac)$_3$phen] (Figure 1b). The metal position occupancy was refined to the following values: 85.5(8)% of Y^{3+} and 14.5(8)% of Tb^{3+}. It was impossible to highlight the presence of Eu^{3+}, as its proportion during synthesis was of the order of 1% (molar). However, its presence was confirmed by optical measurements (Section 2.2). The data on the crystal lattice are given in Table S1. All C-O bond lengths in the complex are close to each other, ranging from 1.26(1) Å to 1.271(9) Å (Table S2), confirming that the charge, once the ligand is deprotonated by the base, is delocalized

throughout the β-diketone. All Tb/Y-O bond lengths, from 2.300(5) Å to 2.333(5) Å, and Tb/Y-N bond lengths, from 2.534(6) Å to 2.565(6) Å, agree with those already reported in the literature.[67,82] The Ln^{3+} ion is in a {O6N2} environment that can be likened to a square antiprism (D4d, Table S3). The shortest Tb/Y…Tb/Y distance is equal to 8.003 Å along the [011] direction within the unit cell (Figure 1c). The homogeneity of the Ln^{3+} dispersion was confirmed by EDX analysis of the [$Eu_{15}Tb_{85}$], [$Eu_{0.01}Tb_{0.20}Y_{0.79}$] and [$Eu_{0.01}Tb_{0.10}Y_{0.79}$] complexes as an example, as shown in Figure S2 and Table S4.

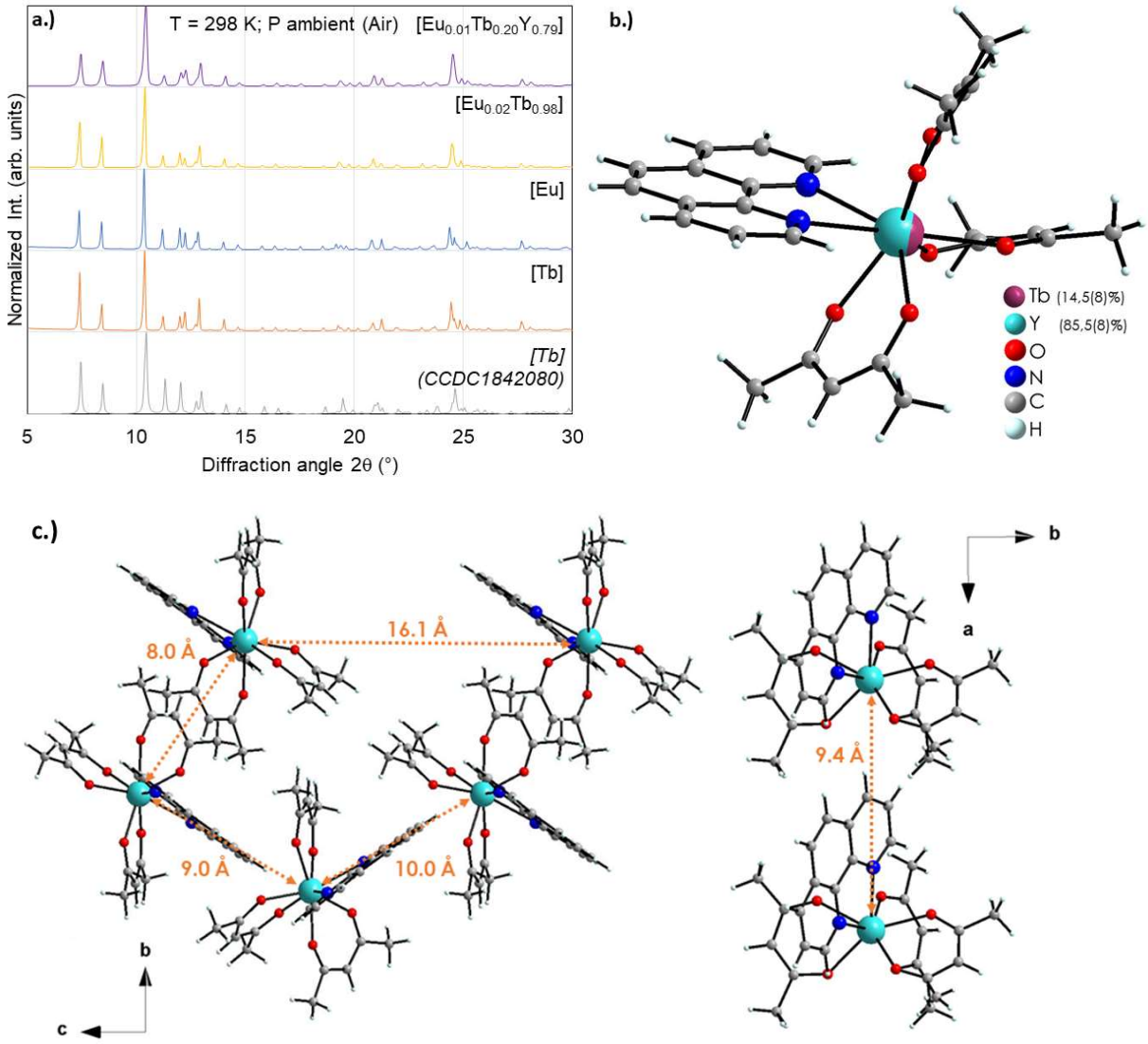

Figure 1: a) X-ray diffraction patterns of [Ln(acac)$_3$phen] with different compositions, reference [Tb(acac)$_3$phen] (CCDC 1842080) from Bukvetskii *et al*.[67]. b) Molecular structure of [$Eu_{0.01}Tb_{0.20}Y_{0.79}$(acac)$_3$phen]; c) Distances between the Ln atoms.

The structure of the studied complex [Ln(acac)$_3$phen] (Ln = Y, Tb, Eu) is not affected by the Eu/Tb/Y proportion. The presence of organic ligands (acac and phen) is also confirmed by FTIR analysis (Figure S3), which should optimize the emission of the complex,[32,63,72,64–71] whereas the interionic distance between Tb-Eu should be close enough to allow energy transfer (ET).[4,5,65,76–80]

2.2 Photoluminescent properties

2.2.1 Energy transfer between Tb-Eu and the antenna effect in the complex: Emission and excitation spectra

Under excitation at 405 nm, the complexes [Eu], [Tb], [$Eu_{0.02}Tb_{0.98}$], and [$Eu_{0.01}Tb_{0.20}Y_{0.79}$] exhibit effective emissions due to the '*Antenna effect'* of the organic ligand in the visible range, as shown in Figure 2a. Furthermore, the strong Eu^{3+}emission can be observed even at low Eu^{3+} concentrations in the complex, so it can be assumed that the presence of Tb^{3+} optimizes the Eu^{3+} emission through energy transfer between them.

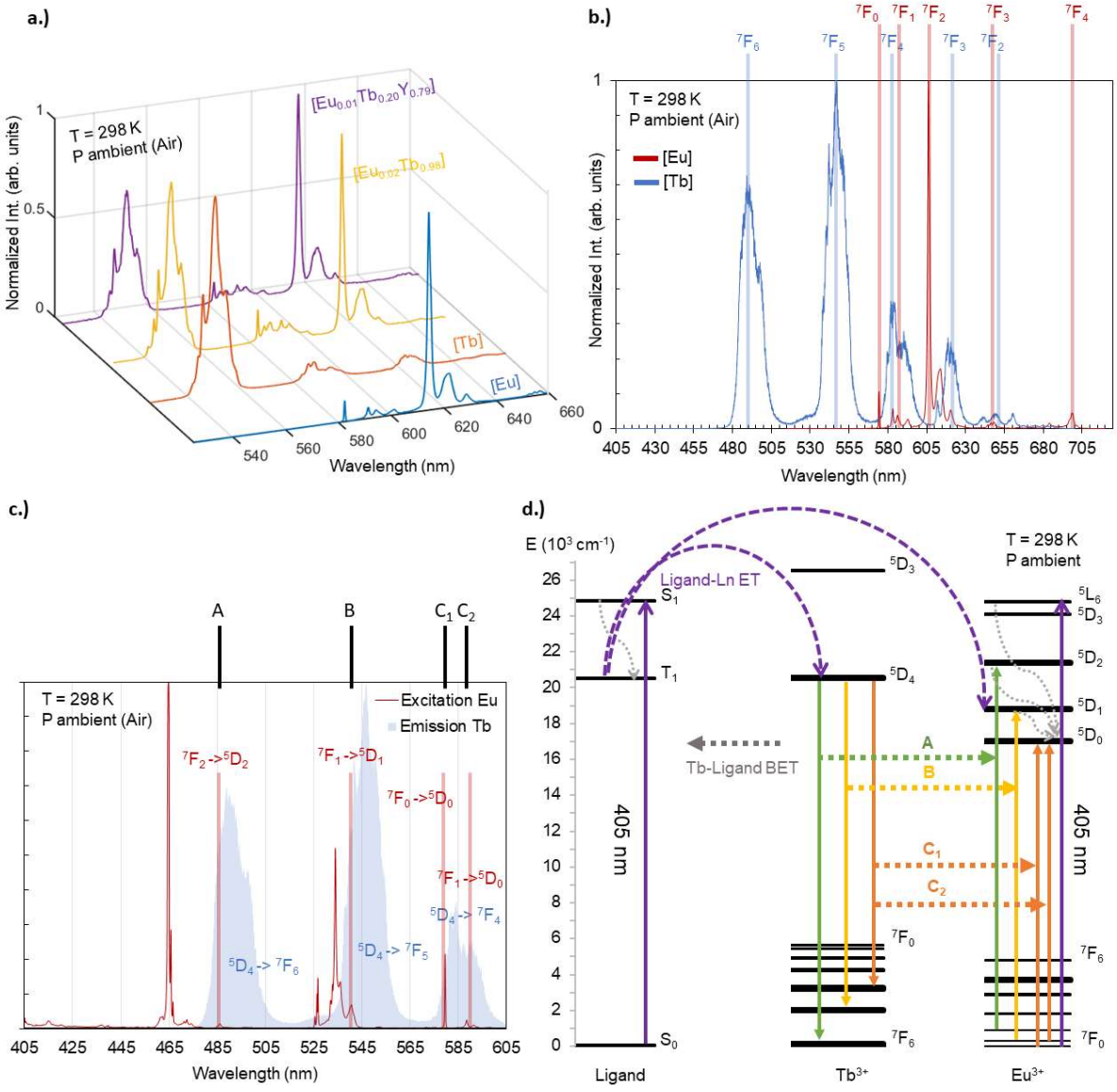

Figure 2: a) Emission spectra of [Eu(acac)$_3$phen], [Tb(acac)$_3$phen], [$Eu_{0.02}Tb_{0.98}$(acac)$_3$phen], and [$Eu_{0.01}Tb_{0.20}Y_{0.79}$(acac)$_3$phen] at 405 nm excitation at room temperature. b) Emission spectra of [Eu(acac)$_3$phen] in red and [Tb(acac)$_3$phen] in blue, with the main energy transitions ($^5D_0$ (Eu^{3+}) and from $^5D_4$ (Tb^{3+}) written in red and in blue, respectively). c) Overlay of the Tb^{3+} emission spectrum

(blue) with Eu^{3+} excitation spectrum of the emission at 612 nm, for transition $^5D_0 \rightarrow {}^7F_2$ (red line) in their pure complex, the assignment of the corresponding transitions of Eu^{3+} (in red) and Tb^{3+} (in blue), and the overlap noted as transitions A, B, C_1 and C_2. d) Proposed energy transfer pathways under 405 nm laser excitation.

The emission spectra of the [Eu] and [Tb] complexes under 365 nm excitation are shown in Figure 2b. The emissions of Eu^{3+} from $^5D_0$ are at 574 nm (to $^7F_0$), 580–590 nm (to $^7F_1$), 600–625 nm (to $^7F_2$), and 695–705 nm (to $^7F_4$). The emissions of Tb^{3+} from $^5D_4$ are at 480–510 nm (to $^7F_6$), 535–560 nm (to $^7F_5$), 575–600 nm (to $^7F_4$), 610–630 nm (to $^7F_3$), and 635–660 nm (to $^7F_2$), respectively. The main intense peak of Eu^{3+} (612 nm) partially overlaps with a Tb^{3+}emission peak (615 nm). In Figure 2c, the emission spectrum of Tb^{3+} is superimposed on the excitation spectrum of Eu^{3+} in its pure complex. The excitation spectrum of Eu^{3+} shows its main absorption: centered at 410 nm ($^7F_2$ to $^5D_3$), 465 nm ($^7F_0$ to $^5D_2$), 485 nm ($^7F_2$ to $^5D_2$), 525 nm ($^7F_0$ to $^5D_1$), 535 nm ($^7F_1$ to $^5D_1$), 580 nm ($^7F_0$ to $^5D_0$), and 590 nm ($^7F_1$ to $^5D_0$). Very intense and broad absorption bands below 420 nm, from 220 to 410 nm, are also observed (Figure S4), and are attributed to the absorption of ligands. The absorption of Eu^{3+} in complex [Eu] from $^7F_0$ to $^5L_6$ is shown at 400 nm. Therefore, upon 405 nm excitation, the ligand will be excited, as well as the Eu^{3+}.

In the emission spectrum of Tb^{3+}, four main overlaps with the excitation spectrum of $Eu^{3+}$are observed. According to the theory of Förster and Dexter,[42,44] these transitions centered at 486 nm, 540 nm, and 585 nm could be considered as the main pathways for Tb^{3+}-Eu^{3+} ETs at room temperature: $^5D_4 \rightarrow {}^7F_6 = {}^7F_2 \rightarrow {}^5D_2$, $^5D_4 \rightarrow {}^7F_5 = {}^7F_1 \rightarrow {}^5D_1$, and $^5D_4 \rightarrow {}^7F_4 = {}^7F_0$ (or $^7F_1$) $\rightarrow {}^5D_0$, respectively. These possible energy transfer pathways are denoted for simplicity as ET A, B, C_1, and C_2 in the proposed ET mechanism (Figure 2d).

The excitation spectra of Eu^{3+} and Tb^{3+} are then analyzed at room temperature and at low temperature in the complex at different Ln^{3+} concentrations to analyze the impact of temperature on Tb^{3+}-Eu^{3+} ET. At low temperature, Eu^{3+} electrons can be de-excited from the $^7F_2$ or $^7F_1$ to $^7F_0$, making ET pathways A or even B and C_2 impossible. At room temperature, the [Eu] and [Tb] complexes absorb energy from the organic ligand, as shown by a broad excitation band (405–420 nm)[28,85] at the top of Figure 3a & 3b, respectively. In the [Eu] complex, upon irradiation at 405 nm, electrons can be excited to level $^5L_6$, but there are no excited levels at this position for the [Tb] complex (Figure 2d). Thus, after excitation at 405 nm, Eu^{3+} can be excited by the organic ligand to the $^5D_1$ level[71,86–89] or irradiation to level $^5L_6$, whereas Tb^{3+} can be excited only by the energy transferred from the organic ligand (Figure 2d).[32] The excitation spectra of the complexes [$Eu_{0.02}Tb_{0.98}$] and [$Eu_{0.01}Tb_{0.2}Y_{0.79}$] are shown in the middle and bottom of Figure 3, respectively. Here, compared to the [Eu] complex, the presence of Tb^{3+} adds an intense absorption peak centered at 485 nm, corresponding to the transition of Tb^{3+} from $^7F_6$ to $^5D_4$. However, the presence of Eu^{3+} does not have a significant impact on the Tb^{3+} excitation spectra, meaning that the back-energy transfer (BET) of Eu^{3+} to Tb^{3+} is negligible in this current complex.

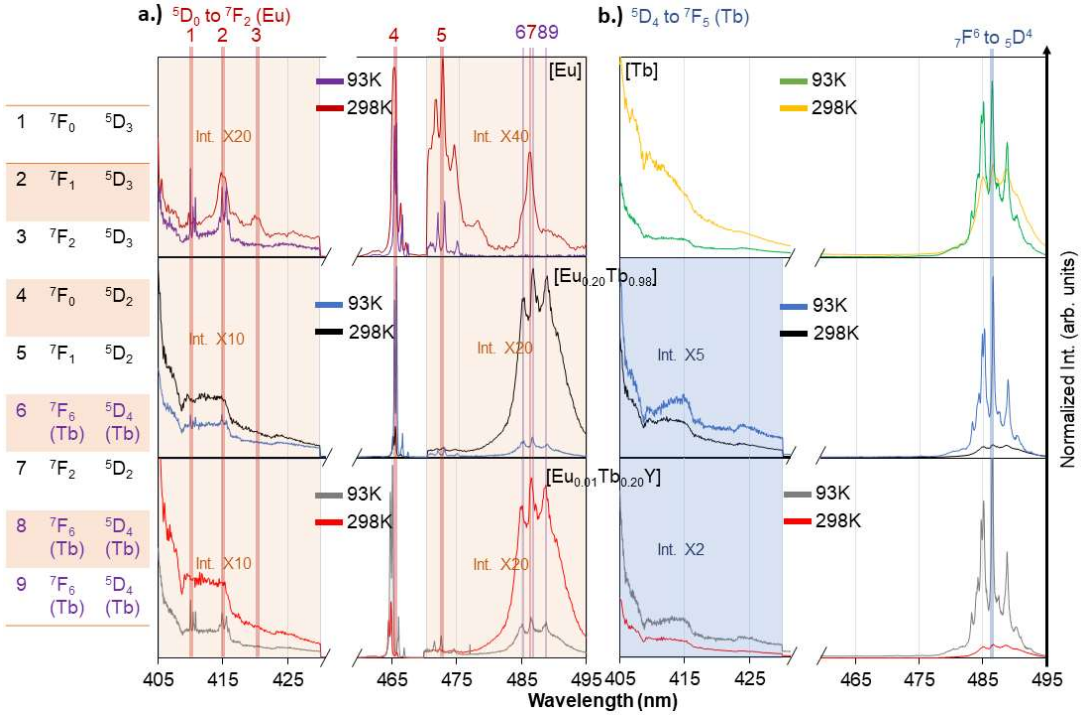

1	$^7F_0$	$^5D_3$
2	$^7F_1$	$^5D_3$
3	$^7F_2$	$^5D_3$
4	$^7F_0$	$^5D_2$
5	$^7F_1$	$^5D_2$
6	$^7F_6$ (Tb)	$^5D_4$ (Tb)
7	$^7F_2$	$^5D_2$
8	$^7F_6$ (Tb)	$^5D_4$ (Tb)
9	$^7F_6$ (Tb)	$^5D_4$ (Tb)

Figure 3: Excitation spectra of a) Eu^{3+} (emission 612 nm for the transition $^5D_0$ to $^7F_2$) and b) Tb^{3+} (emission 550 nm for the transition $^5D_4$ to $^7F_5$) in their pure complexes, and in $[Eu_{0.02}Tb_{0.98}(acac)_3phen]$ and $[Eu_{0.01}Tb_{0.2}Y_{0.79}(acac)_3phen]$ at 298 K and 93 K; The peak distributions of Eu^{3+} are presented in the table inserted. (The 'Int. X N' stands for Normalized intensity times, N)

The impact of temperature can be observed in the overall excitation spectra of the [Eu] complex: the excitation intensity decreases considerably at 93 K compared to room temperature, whereas the excitation pathways from level $^7F_2$ disappear (peaks 3 and 7) as expected. The same peaks also disappear in the $[Eu_{0.02}Tb_{0.98}]$ and $[Eu_{0.01}Tb_{0.2}Y_{0.79}]$ complexes. The absorption of the organic ligand toward Tb^{3+} decreases at 93 K (Figure 3b, top). The effects of temperature on the Tb-Eu ET can also be observed in the $[Eu_{0.02}Tb_{0.98}]$ and $[Eu_{0.01}Tb_{0.2}Y_{0.79}]$ complexes. The Tb^{3+}absorption (peaks 6, 8 and 9, in the violet line) decreases significantly in the Eu^{3+} excitation spectra at low temperature due to the reduction in ET from Tb^{3+} (Figure 3a, middle and bottom). Furthermore, an increase in the overall excitation intensity of Tb^{3+}, and more significant at 486 nm (Figure 3b) allows us to confirm this deduction (Figure 3b, middle and bottom). Here, upon excitation at 405 nm, the cross-relaxation of Tb^{3+} is not considered, because the highest energy level reached by Tb^{3+} through the ET ligand will be the $^5D_4$ level. However, cross-relaxation of Eu^{3+} should be observed when the Eu concentration is high.[76] However, these processes will not be problematic for our future experiments given the low concentration of Eu in the complex.

2.2.2 Impacts of Ln^{3+} composition on Tb-Eu ET: Time-resolved measurements

Upon excitation at 405 nm, the organic ligands are activated, and the electrons from the S_1 state then move to the T_1 state through nonradiative relaxation or IC, for further ET to Ln^{3+} (L-M). Based on previous structural analysis, we assume that the distance between ligands is too great for π-π interaction to occur, and therefore there is no ET between the ligands in this system.[28,90] As mentioned earlier, both Tb^{3+} and Eu^{3+} accept the energy transferred from the organic ligand to reach

their excited state, Tb^{3+} to $^5D_4$ and Eu^{3+} to $^5D_2$, respectively. Furthermore, Eu^{3+} can also be partially excited by laser irradiation at the same wavelength. Subsequently, the excited electrons of Ln^{3+} are deactivated through radiative decay or ET. The interaction between the ligand and the emitted center, Ln^{3+}in this case, enhances Ln^{3+} emission upon ligand excitation, a phenomenon typically referred to as the '*antenna effect*'. As observed previously, with 405 nm irradiation, ligand absorption is intense in the excitation process of both Tb^{3+} and Eu^{3+}. Considering the energy transfer between Tb^{3+}-Eu^{3+} in the system, Eu^{3+} could be excited by a) direct irradiation with a 405-nm laser, b) ligand-Eu^{3+} ET, or c) Tb^{3+}-Eu^{3+} ET. Furthermore, other nonradiative ET pathways must also be considered.[40]

Intermolecular Tb^{3+}-Eu^{3+} ET with different composition [EuTb]

In Figure 4a and b, the lifetimes of Tb^{3+} and Eu^{3+} are shown for different Eu^{3+} concentrations, respectively. The rise time of Tb^{3+} has not been observed because the ligand-Tb^{3+} ET is too fast (in the nanoseconds range).[28,91] However, a rise time of Eu^{3+} is presented in Figure 4b, thus besides the fast ligand-Eu^{3+} ET, the Ln^{3+}-Ln^{3+} ET occurs with Eu^{3+} as an acceptor. At room temperature, interionic ET between Tb^{3+} and Eu^{3+} is an important mechanism when the interionic distance is smaller than the critical distance R_0.[76,77] The considerable reduction in the decay time of the Tb^{3+} emission in complexes with Eu^{3+} indicates the transfer of energy from the $^5D_4$ level of Tb^{3+} to excite Eu^{3+}.[65,90,92] Figure 4a shows that the decay time of Tb^{3+} emission decreases with increasing Eu^{3+} concentration, corresponding to the same variation in Eu^{3+} rise time (Figure 4b), which can be described by the simplified model equation 1: [5,78,79,93–95]

$$n = \left[n_0 + n_1\left(1 - \exp\left(\frac{-t}{\tau_1}\right)\right)\right]\exp\left(\frac{-t}{\tau_2}\right)$$

eq. 1

Where n and n_0 are the number of electrons in the excited level at time t ant t_0, respectively; τ_2 is the decay time from the upper level; n_1 presents the number of electrons in the feeding level; and τ_1 is the time for feeding this level. This model will be used to fit the Eu^{3+} decay-time curves (Equation S1), where τ_1 is the decay time of Tb^{3+}, fitted by the biexponential decay function (Equation S2). The fitted curve is shown in Figure S5 for all the complexes and values are reported in Table 1. The fitted decay time for Tb^{3+} (transition $^5D_4 \rightarrow {}^7F_5$ at 550 nm) and Eu^{3+} (transition $^5D_0 \rightarrow {}^7F_2$ at 612 nm) in their pure complexes agree well with reported values.[79,96,97]

Table 1: Fitted lifetime of Tb^{3+} and Eu^{3+} in the complexes in air and in N_2, Tb^{3+} emission at 550 nm and Eu^{3+} emission at 612 nm under 405 nm excitation.

Fitted lifetime (ms)	In air				Under 1 atm N_2			
Sample	τ(Tb)	R^2_A	τ(Eu)	R^2_B	τ(Tb)	R^2_A	τ(Eu)	R^2_B
[Tb]	0.7143	0.9971			0.7143	0.9975		
[Eu]			0.7131	0.9997			0.7087	0.9998
$[Tb_{0.20}Y_{0.80}]$	0.7143	0.9722			0.7143	0.9974		
$[Tb_{0.10}Y_{0.90}]$	0.6805	0.9991			0.7143	0.9962		
$[Tb_{0.05}Y_{0.95}]$	0.4310	0.9967			0.6646	0.9975		
$[Tb_{0.005}Y_{0.995}]$	0.4005	0.9981			0.7135	0.9985		
$[Eu_{0.20}Y_{0.80}]$			0.6795	0.9998			0.6677	0.9998
$[Eu_{0.02}Y_{0.98}]$			0.7143	0.9974			0.7143	0.9973
$[Eu_{0.005}Y_{0.995}]$			0.7091	0.9955			0.6972	0.9932
$[Eu_{0.15}Tb_{0.85}]$	0.2225	0.999	0.7434	0.9792	0.2243	0.9989	0.746	0.9786
$[Eu_{0.02}Tb_{0.98}]$	0.4481	0.9996	0.7692	0.9914	0.4497	0.9996	0.7042	0.9904
$[Eu_{0.01}Tb_{0.99}]$	0.6632	0.9969	0.7692	0.9869	0.6761	0.9944	0.7692	0.9866
$[Eu_{0.005}Tb_{0.995}]$	0.6632	0.9969	0.7692	0.9869	0.6761	0.9944	0.7692	0.9866
$[Eu_{0.01}Tb_{0.20}Y_{0.79}]$	0.4252	0.9985	0.7404	0.9922	0.4315	0.9977	0.7452	0.9920
$[Eu_{0.01}Tb_{0.10}Y_{0.89}]$	0.3984	0.9722	0.6530	0.9806	0.4317	0.9842	0.7033	0.9879
$[Eu_{0.01}Tb_{0.01}Y_{0.98}]$	0.1132	0.9881	0.5765	0.9628	0.1001	0.7002*	0.6227	0.9697

*Fitted R^2 not satisfactory due to the extremely small quantity of Tb^{3+} in the complex $[Eu_{0.01}Tb_{0.01}Y_{0.98}]$, the curve can be found in Figure S5.

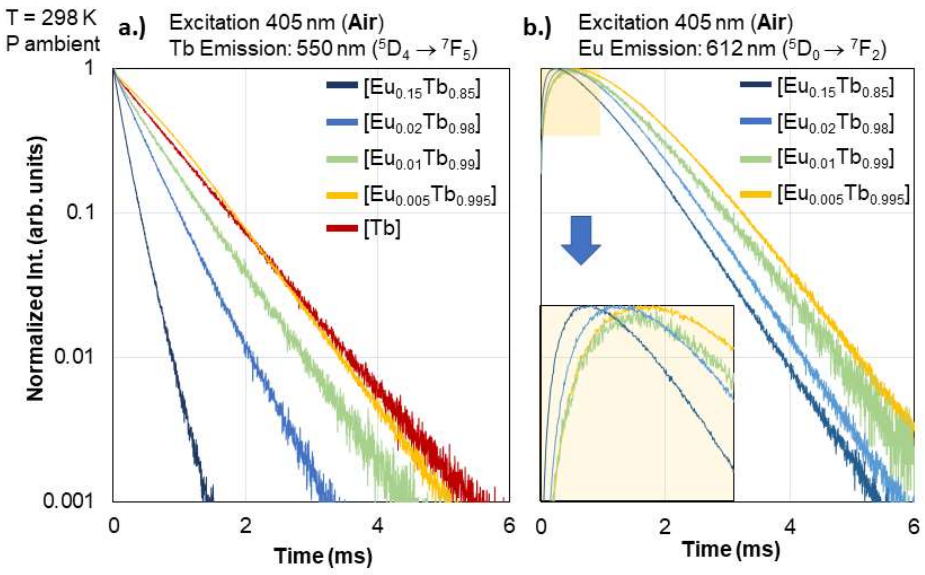

Figure 4: Lifetime measurements of a) Tb^{3+} and b) Eu^{3+} in complex $[Eu_xTb_{1-x}(acac)_3phen]$.

Therefore, in a system with such a high concentration of Tb^{3+} relative to Eu^{3+}, Tb^3-Eu^{3+} ET still occurs even if the concentration of Eu^{3+} is low (0.5 mol %). It can be considered that the doped Eu^{3+} ions are always surrounded by their sensitizer (Tb^{3+}). Thus, the more Eu^{3+} in the complex, the more Tb^{3+} ions are deactivated by Eu^{3+}, resulting in a decrease in Tb^{3+} decay time with increasing Eu^{3+} concentration (from 0.66 to 0.22 ms) (Table 1). Furthermore, assuming that the proportion of excited Tb^{3+} ions via non-radiative relaxation is negligible, the rise time of Eu^{3+} is equal to the Tb^{3+} decay time, which corresponds to the feeding time of Eu^{3+} by Tb^{3+}. However, the decay time of Eu^{3+} is not significantly influenced by the presence of Tb^{3+}(Table 1).

Addition of yttrium as an optical diluent

The impact of the Y^{3+} diluent on the Tb^{3+}-Eu^{3+} ET was studied in different compositions. First, lifetime measurements of Tb^{3+} of the complex were performed. As shown in Figure 5a and Table 1, the Tb^{3+}decay time of [Tb] is identical to that of $[Tb_{0.2}Y_{0.8}]$, and from 80 mol.% of Y^{3+}, increasing the dilution by Y^{3+} leads to a decrease in the Tb^{3+} decay time (from 0.68 to 0.40 ms). The decrease in Tb^{3+} decay time has also previously been observed due to adding Eu^{3+}, which has been assumed to be an indicator of ET. As there is no ion acceptor in $[Tb_xY_{1-x}]$ complexes, O_2 present in air may be the main cause of the decrease in Tb^{3+} decay time, because the presence of O_2 disrupts the ligand-Ln^{3+} ET because O_2 replaces Ln^{3+} as an energy acceptor. When the O_2 molecule is close enough to the ligand to activate energy quenching, rather than exciting Ln^{3+}, the ligand transfers energy to the triplet state of O_2. This phenomenon is known as O_2 quenching in ligand-excited phosphor.[9,59] Because of O_2 quenching, the highly diluted (>80 mol %) complex shows significant reductions in the Tb^{3+} decay time (from 0.42 to 0.11 ms). As the Y^{3+} concentration increases, the Tb^{3+} concentration decreases in the $[Tb_xY_{1-x}]$ complex, and under ambient pressure in air, the O_2 quenching effect is greater at lower Tb^{3+} concentrations.

Subsequently, 1 mol % Eu^{3+} was added to the system, and the Tb^{3+} lifetime was measured for the complexes $[Eu_{0.01}Tb_xY_{0.99-x}]$, where x = 0.99, 0.20, 0.10, and 0.1. As shown in Figure 5b, adding 1 mol % Eu^{3+} in the dilute system further decreases the Tb^{3+} decay time, besides interfering with O_2 quenching.

The reduction in Tb^{3+} decay time is greater with increasing Y^{3+} concentration (Table 1). The reason may be that the decrease in Tb^{3+} concentration makes Tb^{3+}-Eu^{3+} ET more efficient, or when the O_2-quenching effect is greater, or both. Therefore, to reduce the O_2-quenching effect, the sample was confined in a closed cell for 5 min of N_2 flow to minimize the O_2 concentration in the measurement environment. Lifetime measurements were again performed for the complex at the same compositions under N_2 flow. As shown in Figure 5c and in Table 1, in contrast to the previous measurement in air, the Tb^{3+} decay curves under N_2 are all identical regardless of the Tb^{3+} concentration and are identical to the Tb^{3+} decay curve in [Tb] in air. This is because O_2 quenching causes Tb^{3+} decay time to decrease and the N_2 atmosphere has reduced O_2 quenching. Furthermore, when O_2 quenching no longer disrupts the ligand-Tb^{3+} interaction, Eu^{3+}-induced decreases in Tb^{3+} decay times are still observed (from 0.67 to 0.22 ms), but they are slightly lower than measurements in air (Figure 5d & Table 1). Therefore, O_2 quenching does not affect the Tb^{3+}-Eu^{3+} ET in the complex.

The change in atmosphere will not have a significant impact on the Eu^{3+} decay time (Table 1) regardless of the Eu^{3+} concentration because Eu^{3+} can also be excited by the 405 nm laser (Figure 2d). As shown in Figure S6 and Table 1, even the Eu^{3+} decay time in [$Eu_{0.05}Y_{99.5}$] (0.71 ms) is identical to that in [Eu] (0.71 ms), as expected. Furthermore, we noted in Table 1, Figure 5a and 6c that O_2-quenching interference was only significant at low Tb^{3+} concentration (<20%). To confirm this hypothesis, the measurement of the lifetime of [Eu_xTb_{1-x}], where x = 0.15; 0.02; 0.01; 0.005; and 0, in the N_2 atmosphere was also performed (Table 1 and Figure S7) to complement the previous measurement in Figure 4, which shows a negligible difference compared to the measurement in the air. As expected, O_2 quenching has no significant effect on the undiluted system [Eu_xTb_{1-x}].

In the Y^{3+}-diluted system, it was found that Tb^{3+}-Eu^{3+} ET still occurs even at low Tb^{3+} concentration, with a reduction in Tb^{3+} decay time (0.11 ms, Table 1), and Eu^{3+} rise time observed in the [$Eu_{0.01}Tb_{0.01}Y_{0.98}$] complex (Figure 5d and S8, respectively). Therefore, Tb^{3+}-Tb^{3+} energy migration may play a critical role in highly dilute systems on the enhancement of Tb^{3+}-Eu^{3+} ET efficiency. Furthermore, increasing the concentration of Y^{3+} decreases the Tb^{3+} decay time (Figure 5d and Table 1) and the Eu^{3+} rise time (Figure S8), which theoretically stands for the optimization of Tb^{3+}-Eu^{3+} ET efficiency. However, in this study, increasing the concentration of Y^{3+} leads to a reduction in the absolute emission intensity of Tb^{3+} and Eu^{3+}. This observation was not quantified using an emission intensity reference. Therefore, the decrease in Tb^{3+} decay time and the Eu^{3+} rise time may be caused by other quenching effects, but not the increase in Tb^{3+}-Eu^{3+} ET efficiency.

In conclusion, dilution with Y^{3+} induces a decrease in the Tb^{3+} concentration, which amplifies the O_2-quenching effect and leads to a reduction in the emission intensity of both Tb^{3+} and Eu^{3+}. To date, dilution with Y^{3+} has only exhibited a negative impact on the photoluminescent emission of the complex. However, in a highly concentrated Tb^{3+} or Eu^{3+} system, the concentration quenching phenomenon must be carefully considered.[40,43,85] Dilution with optically neutral ions like Y^{3+} could potentially enhance emission intensity by protecting the emitter from concentration quenching.[98] However, in the current complex, the decay time of Tb^{3+} can still be accurately measured even at high Tb^{3+} concentration (Figure 5a). Furthermore, dilution with Y^{3+} does not affect the Tb^{3+} decay time when O_2 quenching is eliminated (Figure 5c). These results suggest that Tb^{3+} concentration quenching may not be significant enough to be observed in the present system, possibly due to the well-crystallized samples after synthesis, thus the structural defect could be negligible. Although Tb^{3+} concentration quenching has not been observed so far, it should be a concern for further pressure-

sensing applications due to the potential pressure-induced structural defect. Therefore, in Sections 2.3, Y^{3+}-diluted complexes are studied, but only compositions with a high Tb^{3+} concentration (>20 mol %) are considered to minimize interference from O_2 quenching.

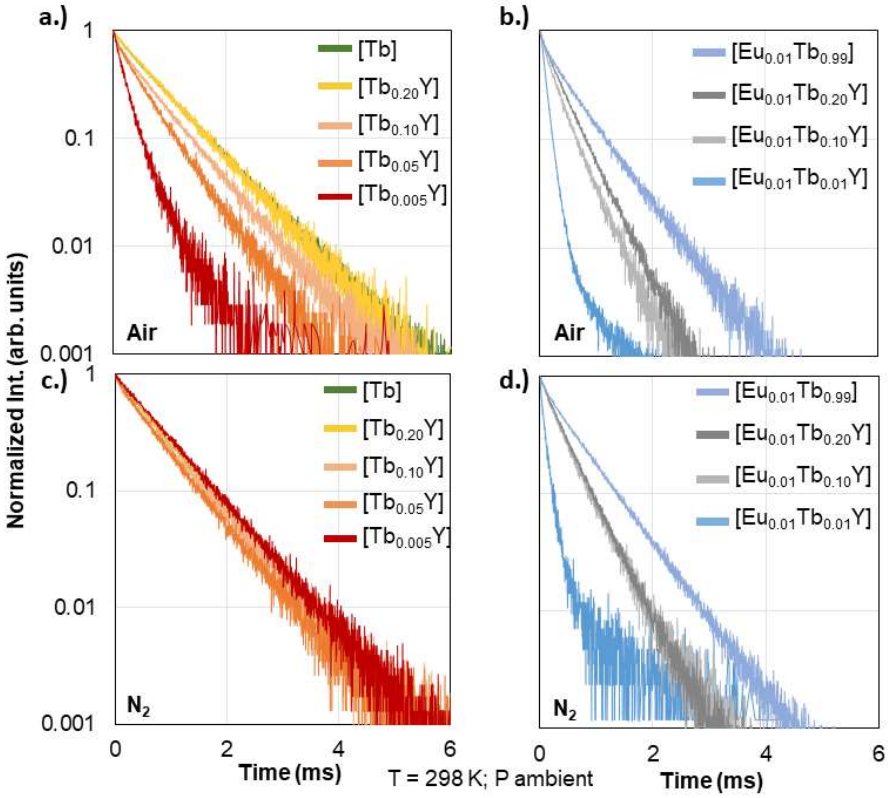

Figure 5: Lifetime measurements of Tb^{3+} in the $[Tb_xY_{1-x}(acac)_3phen]$ complex a). in air and c). under 1 atm N_2; lifetime measurements of Tb^{3+} in the $[Eu_{0.01}Tb_xY_{0.99-x}(acac)_3phen]$ complex b). in air and d). under 1 atm N_2. (Excitation at 405 nm; Tb emission at 550 nm)

2.2.3 Impacts of temperature on energy transfer between Tb^{3+}-Eu^{3+}

Temperature has a significant impact on Tb^{3+}-Eu^{3+} ET. At a given composition, low temperature perturbs the Tb^{3+}-Eu^{3+} ET process due to the depopulation of Eu^{3+} $^7F_2$ or $^7F_1$ levels. To clarify the impact of temperature on the Tb^{3+}-Eu^{3+} ET system, a composition $[Eu_{0.01}Tb_{0.2}Y_{0.79}]$ was chosen as an example. As shown in Figure S9, the energy transferred from Tb^{3+} to Eu^{3+} decreases considerably from room temperature (298 K) to 93 K; therefore, the rise time of Eu^{3+} disappears as the temperature decreases. This observation correlates with the previous results of the Eu^{3+} excitation spectrum at 93 K. The depopulation of the upper level of Eu^{3+} to the initial state eliminates the Tb^{3+}-Eu^{3+} ET pathway: $^5D_4 \rightarrow {}^7F_6 = {}^7F_2 \rightarrow {}^5D_2$, $^5D_4 \rightarrow {}^7F_5 = {}^7F_1 \rightarrow {}^5D_1$, and $^5D_4 \rightarrow {}^7F_4 = {}^7F_1 \rightarrow {}^5D_0$ (ET A, B, and C_2 in Figure 2d, respectively). This causes a significant decrease in the Tb^{3+}-Eu^{3+} ET rate. Furthermore, the impact of temperature on the interaction rate between the ligand and Tb^{3+} has been reported, showing that the rate of the ligand-Tb^{3+} ET decreases with decreasing temperature.[99]

Now that we have established that a significant ET occurs from Tb^{3+} to Eu^{3+} in the complex and that it is not affected by dilution with Y^{3+}, the variation in the photoluminescent properties of these complexes under pressure can be examined. In Section 2.3, the pressure sensitivity based on the

luminescent-intensity-ratio of selected complexes is studied in a diamond anvil cell (DAC) up to a hydrostatic pressure of 1000 MPa. Furthermore, the effect of temperature on pressure sensitivity is also considered in the context of applications for pressure-temperature (P-T) sensing.

2.3 Luminescent-intensity-ratio based pressure sensing

The luminescent-intensity-ratio (LIR), or relative emission intensity, is a widely used parameter in optics. Calculating the ratio of two distinct emission intensities, the LIR allows for the neglection of any impact on the absolute intensity which might be challenging to control in real measurement. If the interaction between two emissive levels can be influenced by the environment, such as temperature, interionic distance, or the symmetry of the crystal structure, the LIR reflects their response to environmental variation. Therefore, the LIR is considered a popular variable in many sensing applications. In the Tb^{3+} and Eu^{3+} complex, the LIR of the Tb^{3+}/Eu^{3+} emission can be calculated by considering their main peaks; the Tb^{3+} peak (at 540 nm, zone A) and the Eu^{3+} peak (620 nm, zone C) as shown in Figure 6a. In the present complex, assuming that the dispersion of Ln^{3+} is homogenous in the entire crystal, and that all the Eu^{3+} are excited by energy from Tb^{3+}-Eu^{3+} ET, the LIR represents the ratio of Tb^{3+} electrons deactivated through radiative relaxation to those deactivated through Tb^{3+}-Eu^{3+} ET. Therefore, at room temperature, in the complex at a given concentration of Tb^{3+} and Eu^{3+}, the LIR could be a parameter to quantify the amount of energy transferred from Tb^{3+} to Eu^{3+}.

To understand the impact of structure on the Tb-Eu ET process in the complex, the LIR is then used as a reliable variable to quantify the Tb^{3+}-Eu^{3+} ET. First, the influence of the Ln^{3+} concentration is studied, the LIR of Tb^{3+}/Eu^{3+} is plotted as a function of the Eu^{3+} concentration at room temperature (298 K), with different concentrations of Y^{3+} as the diluent in Figure 6b. The LIR strongly depends on the Eu^{3+} concentration: when the Eu^{3+} concentration ranges between 0 and 5 mol %, the LIR decreases rapidly with increasing % Eu. However, compared to the effect of Eu^{3+} concentration, the diluent Y^{3+} concentration has a negligible impact on the LIR value. The conclusion is consistent with the previous results on decay time.

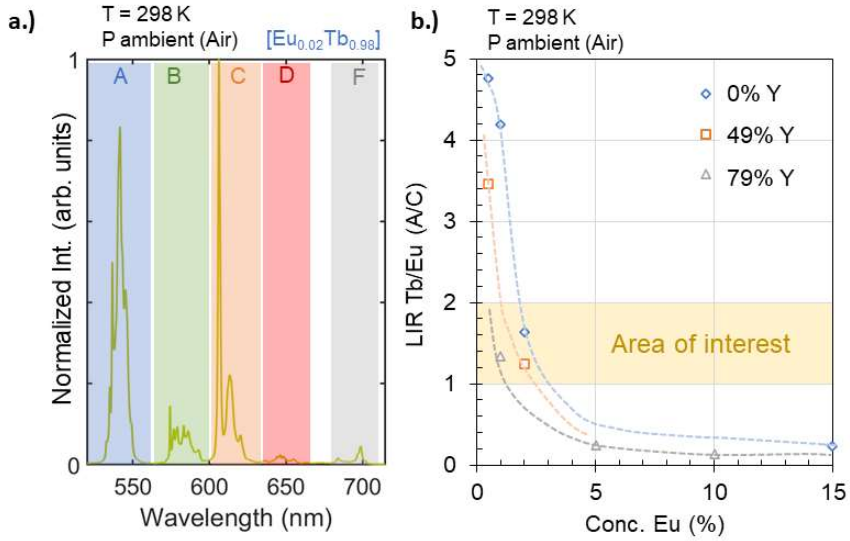

Figure 6: a) Distribution of the emission peak in the complex [$Eu_{0.02}Tb_{0.98}(acac)_3phen$]: A for $^5D_4$ to $^7F_5$ (Tb^{3+}), B for $^5D_0$ to $^7F_{0\&1}$ (Eu^{3+}) and $^5D_4$ to $^7F_4$ (Tb^{3+}), C for $^5D_0$ to $^7F_2$ (Eu^{3+}) and $^5D_4$ to $^7F_3$ (Tb^{3+}), D for $^5D_0$ to $^7F_3$ (Eu^{3+}) and $^5D_4$ to $^7F_{2\&1}$ (Tb^{3+}), and F for $^5D_0$ to $^7F_4$ (Eu^{3+}). b) Calculated luminescent-intensity-ratio (LIR) at different compositions at 298 K with the estimated trend lines in the dotted line, the area of interest with 1 < LIR < 2.

Impact of pressure on energy transfer between Tb^{3+}/Eu^{3+}

According to the previous conclusion, at a given temperature and in the same composition as Ln^{3+}, the luminescent intensity ratio (LIR) depends on the significance of the Tb^{3+}-Eu^{3+} ET process that occurred in the system. The expectation is that a decrease in the interionic distance of Tb^{3+}-Eu^{3+} leads to a significant increase in the Tb^{3+}-Eu^{3+} ET rate based on the FRET theory,[44,76] resulting in a decrease in the LIR Tb/Eu. In the spectrum presenting both Tb^{3+} and Eu^{3+} emission, the Tb^{3+}-Eu^{3+} ET rate should be reflected by the LIR. For reliability, the Ln^{3+} concentration must be selected according to the suitable LIR value, which cannot be extremely large or small to avoid significant uncertainty caused by low emission intensity. Therefore, an area of interest is chosen with a LIR value between 1 and 2 (Figure 6b). Among the three candidates, the compositions [$Eu_{0.02}Tb_{0.98}$] and [$Eu_{0.01}Tb_{0.2}Y_{0.79}$] were selected for further analysis of structural variation. Crystals are compressed in a diamond anvil cell (DAC), confined by a pure solvent (Squalane), under hydrostatic pressure up to 1000 MPa at 20 °C (293 K). The liquid-confined medium of the crystal allows for the elimination of the presence of O_2, thus protecting the crystal from luminescence quenching. As shown in Figure 7a and 7c, the emission intensity of Tb^{3+} (A for the $^5D_4$ to $^7F_5$ transition, at 550 nm) decreases whereas the intensity of Eu^{3+} (C for the $^5D_0$ to $^7F_2$ transition, at 612 nm) increases with increasing applied pressure in both complexes. Since the concentration and temperature remain constant during the measurement, the change in structure should be the only reason for the variation in emission intensity. The decrease in Tb^{3+} emission intensity with increasing pressure could be due to that the optimization of the efficiency of Tb^{3+}-Eu^{3+} ET when the Tb^{3+}-Eu^{3+} distance is shortened.

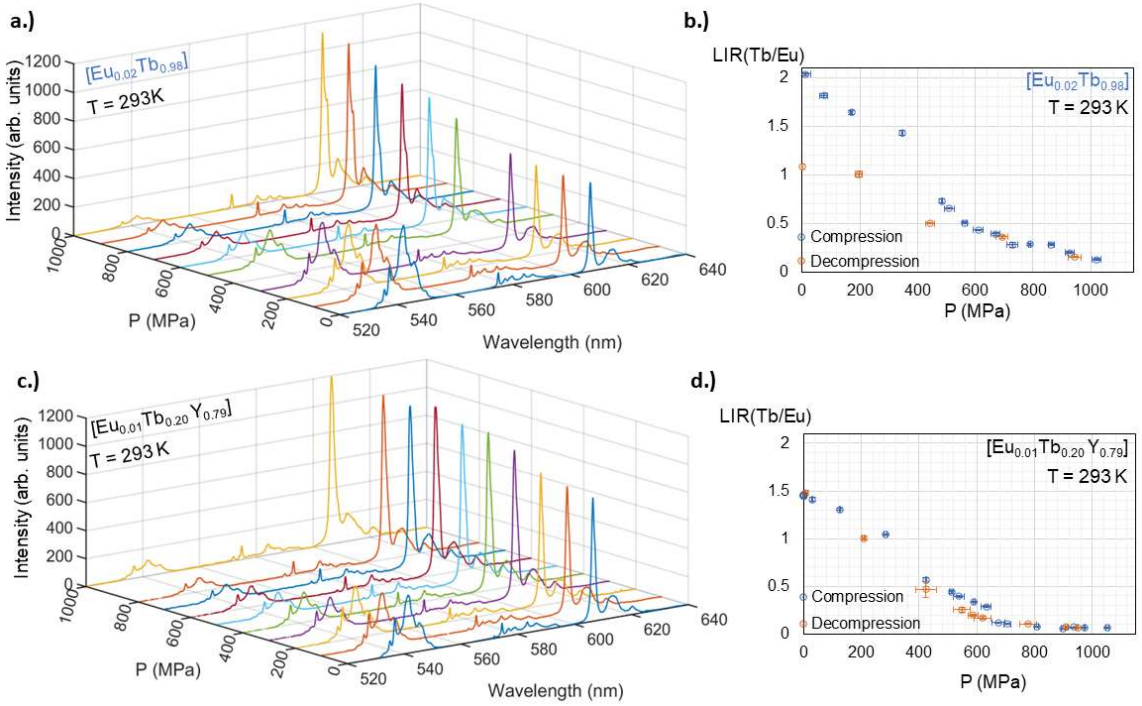

Figure 7: Emission spectra under hydrostatic pressure (in DAC) up to 1000 MPa for a) $[Eu_{0.02}Tb_{0.98}(acac)_3phen]$ and c) $[Eu_{0.01}Tb_{0.2}Y_{0.79}(acac)_3phen]$, and their calibration curve of calculated LIR as a function of pressure (MPa) in b) and d), respectively. (LIR values are the averages of three subsequent measurements, the error bar is calculated by the standard deviation).

As the overall crystal lattice is assumed to be compressed under pressure, the molecular volume should decrease. This change results in a reduction in intermolecular and interatomic distance as well as a modification of structural symmetry, and the orientations of ligands (geometry and parallelism). All these structural variations lead to changes in ET processes within the system. It's challenging to distinguish the specific structural impacts on each ET process due to the complexity of the ET system.

To address this, the same experience was conducted using a physical mixture of pure Tb^{3+} and Eu^{3+} complexes. When a mixture with 50 wt. % of each complex was used, the emission spectrum exhibited both of their own distinct emissions (Figure 8a), with a LIR = 0.65 at ambient pressure in the DAC. Up to 1000 MPa, no significant changes were observed in the emission spectrum compared to that at ambient pressure, except for slight modifications in the emission peak shape due to structural change in the complex. However, those changes in emission peaks are rarely considered detectable and applicable for pressure sensing in such low pressure ranges. As shown in Figure 8b, the LIR varied randomly with pressure due to the inhomogeneity of the mixture. When using focused laser excitation, the laser spot is relatively small (~µm) and as the DAC reduces its confined volume during compression, it is challenging to maintain the same irradiation position during the measurement. Therefore, the homogeneity of the composition has a significant impact on the LIR values, which can explain the uncertainty obtained in the LIR calibration under pressure (Figure 7d and 8b). Furthermore, isolated Tb^{3+} and Eu^{3+} complexes have a negligible response to pressure (<1000 MPa) in terms of LIR variation. This behavior observed in a physical mixture of pure Tb^{3+} and

Eu^{3+} complexes indicates that the decrease in LIR under increasing pressure arises solely from the Tb^{3+}-Eu^{3+} interaction.

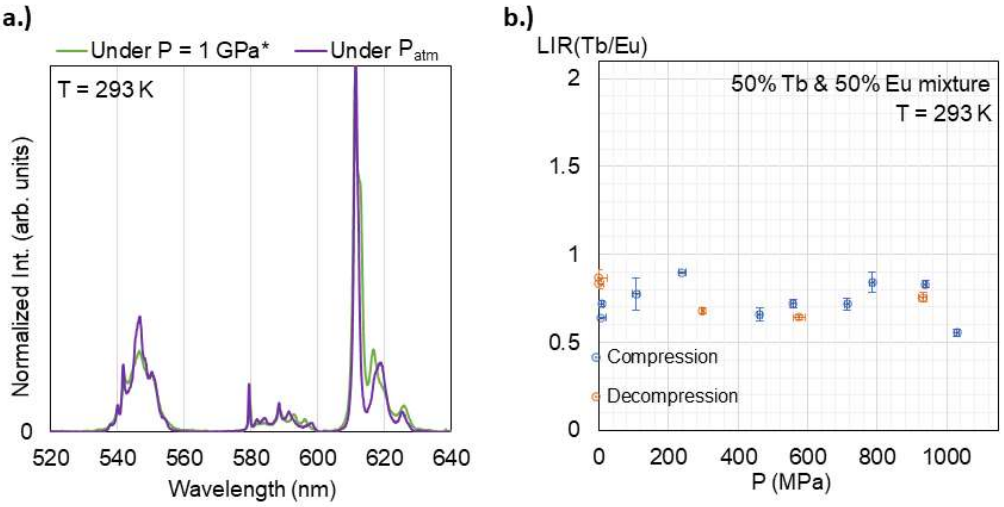

Figure 8: a) Emission spectra under hydrostatic pressure (in DAC) up to 1030 MPa* for a physical mixture of [Eu(acac)$_3$phen] and [Tb(acac)$_3$phen]. b) The calibration curve of the calculated LIR as a function of pressure (MPa). (LIR values are the averages of three subsequent measurements, the error bar is calculated by the standard deviation).

The [$Eu_{0.02}Tb_{0.98}$] complex exhibits a higher LIR pressure sensitivity (Figure 7b) compared to the [$Eu_{0.01}Tb_{0.2}Y_{0.79}$] complex (Figure 7d), resulting in a higher pressure sensitivity. However, both complexes shows limits in pressure sensitivity observed in the disappearance of the Tb^{3+} emission (approximately 700 MPa for both). This behavior is assumed to occur because the original LIR value is different due to the distinct composition of the complex, and the 700 MPa limit for pressure detection is inherently decided by structural flexibility. Unlike the complex with Y^{3+} as a diluent (Figure 7d), the [$Eu_{0.02}Tb_{0.98}$] complex (Figure 7b) shows only partial reversibility of the LIR under pressure up to 1000 MPa. This reversibility could be crucial for pressure measurement applications. Surface defects in the crystal or even slight cracking of the crystal lattice caused by compression should not be overlooked. Furthermore, structural defects may induce luminescence quenching of the Ln^{3+} emitter. The mechanical impact on the luminescent properties of the complex [Tb(acac)$_3$phen] has been reported as triboluminescence.[67] Additionally, the decrease in the intensity of the Eu^{3+}-complex under pressure-induced structural contraction has been observed in previous studies, with authors attributing it to changes in the probability of non-radiative relaxation.[56] Here, the impact of defect quenching could be significant in the high Tb^{3+}concentration complex, but not in the other. We assume that Y^{3+} diluents potentially allow the Tb^{3+} ions to be less trapped in structural defects, enabling good reversibility of the LIR value under pressure. Therefore, the reversibility of the complex may be lost after repeated compressions. It is noted that DAC experiments are limited to three compressions for the same sample due to the elasticity of the nickel seal, and collecting extremely small quantities of the sample after compression is challenging. The reproducibility of the results should be further investigated using other compression equipment. However, it has been verified that when the pressure is increased for the second time, the [$Eu_{0.01}Tb_{0.2}Y_{0.79}$] complex behaves in the same way as when the pressure was increased for the first time (Figure S10).

The relative sensitivity (S_R) to pressure was calculated for both complexes during their first compression, using an equation reported in Szymczak's works[52,100,101] (Equation S3). The S_R was plotted as a function of the pressure up to 700 MPa, as shown in Figure S11. The best relative sensitivity to pressure is 0.1365 %/ MPa and 0.1435 %/MPa for the $[Eu_{0.02}Tb_{0.98}]$ and $[Eu_{0.01}Tb_{0.2}Y_{0.79}]$ complex, respectively, observed around 500 MPa. Due to the significant impact of compression on structural change and, thus, on the Tb^{3+}-Eu^{3+} ET rate, the Tb^{3+}/Eu^{3+} LIR could be an optical tool to reflect slight structural variation, that cannot be precisely observed in structural analysis. This method quantifies slight structural changes at relatively low pressure through the photoluminescence of the material, making it a potential pressure sensor with high sensitivity and reliable reversibility. Compared to the most commonly used methods based on shifting the spectral peak for pressure detection, the LIR method considers all transitions among electronic sublevels by integrating the peak area, simplifying data processing, and thereby optimizing measurement accuracy.

Temperature impacts on pressure-sensing applications

At pressures up to 700 MPa, the luminescent-intensity-ratio of Tb^{3+}/Eu^{3+} in the $[Eu_{0.01}Tb_{0.2}Y_{0.79}(acac)_3phen]$ complex shows remarkable sensitivity to pressure, and this LIR variation induced by the change in the Tb^{3+}-Eu^{3+} interionic distance is reversible. Therefore, the $[Eu_{0.01}Tb_{0.2}Y_{0.79}(acac)_3phen]$ complex can be a potential photoluminescent pressure sensor. Given the use of LIR as a variable, pressure detection is independent of the absolute intensity of emission. As the absolute intensity of emission is affected by the sensor concentration and the equipment parameter (laser power density), the pressure detection is thus not affected by them. However, many studies have highlighted the sensitivity of the Tb^{3+}/Eu^{3+} LIR to temperature,[5,78,102,103] usually applied for thermometry sensor research. Additionally, the impact of temperature can be observed in Figure 6b and Figure 7d, where the LIR value of $[Eu_{0.01}Tb_{0.2}Y_{0.79}(acac)_3phen]$ under ambient pressure varies at different temperatures (298 K (Figure 6b): LIR = 1.32; 293 K (Figure 7d): LIR = 1.46). Therefore, the influence of temperature on pressure sensing in the $[Eu_{0.01}Tb_{0.2}Y_{0.79}(acac)_3phen]$ complex should be thoroughly investigated.

The temperature-induced variation of the Tb^{3+}/Eu^{3+} LIR is often attributed to the thermal population of Eu^{3+} electrons toward its upper level ($^7F_1$ or $^7F_2$). This results from the Tb^{3+}-Eu^{3+} ET process, where higher temperature favors ET from $^7F_2$, decreasing the emission intensity of Tb^{3+} while increasing the emission intensity of Eu^{3+}. Therefore, the Tb^{3+}/Eu^{3+} LIR decreases with increasing temperature. The probability of thermally populated electrons of Eu^{3+} can be described by Boltzmann's distribution.[34,65,104,105] However, the Tb^{3+}/Eu^{3+} LIR can also be influenced by the Tb^{3+}-Eu^{3+} ET rate, which can change with temperature, especially at low temperatures. The temperature calibration of the complex was conducted between 20 and 80 °C to prevent the sample from burning due to the high temperatures. A quasi-linear curve is observed up to 60 °C in Figure S12, following Boltzmann's distribution. This aligns with the results of other studies,[5,65] indicating that Eu^{3+}emission is temperature-sensitive up to 60 °C.

The temperature-induced variation of the LIR cannot be overlooked in the pressure detection by the $[Eu_{0.01}Tb_{0.2}Y_{0.79}(acac)_3phen]$ complex. The isothermal pressure calibrations at four temperatures are shown in Figure 9. The temperature calibration curve under constant ambient pressure, performed outside the DAC at the same temperatures, was plotted to compare the LIR values. Under ambient

pressure, the LIR obtained by the complex measured on a thermal plate for temperature calibration is the same as those confined in the DAC for pressure calibration. A coupled effect between pressure and temperature on LIR is observed (Figure 9). The LIR decreases with increasing pressure as before, but the slope decreases with temperature. The thermal sensitivity of the LIR disappears after 60 °C, which follows the temperature calibration curves, as shown previously. At increasing temperatures, the limit of pressure sensitivity slightly decreases as the initial LIR decreases significantly under ambient pressure.

This result shows that this material can be used as a reliable pressure sensor in an isothermal environment. The working temperature range is confirmed up to 80 °C, limited by the relatively low stability of the organic complex at high temperatures. As the thermal stability of lanthanide complexes could be a limiting factor in the development of such pressure sensor materials, further studies are needed to optimize their thermal stability. Furthermore, as pressure sensitivity is more critical at lower temperature, the minimum working temperature for pressure measurement can be low, as long as the temperature allows the Tb^{3+}-Eu^{3+} ET to occur in the system under ambient pressure. The impacts of temperature on LIR values exist, but they can be easily corrected by pre-calibration of temperature. Although the pressure calibrated curves have not been accurately fitted so far and further studies are required, it can be envisioned that numerous applications of highly accurate pressure sensing by the Ln complex will be inspired by this study.

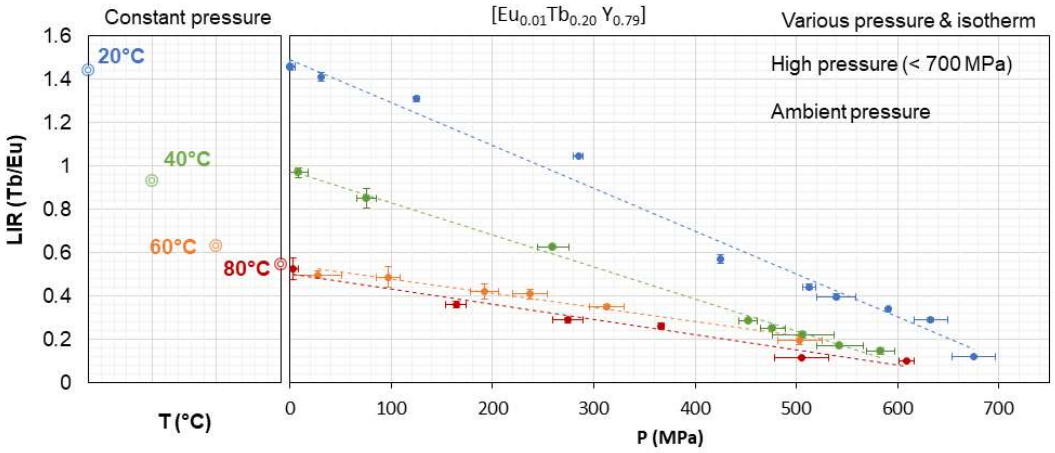

Figure 9: The variation of LIR in complex $[Eu_{0.01}Tb_{0.2}Y_{0.79}(acac)_3phen]$ under constant pressure (ambient pressure outside DAC) and under various pressures in isotherm medium at 20 °C (293 K) in blue, 40 °C (313 K) in green, 60 °C (333 K) in orange, and 80 °C (353 K) in red (in DAC). Error bars are calculated according to the standard deviation over three measurements.

3 Conclusion

In this study, the [Ln(acac)$_3$phen] (Ln = Y, Tb, Eu) complex shows an efficient Tb^{3+}-Eu^{3+} ET process. Upon excitation of the ligand at 405 nm, the impact of structural change on the Tb^{3+}-Eu^{3+} ET was investigated by compressing the complex in a DAC. At up to 700 MPa, the [$Eu_{0.01}Tb_{0.2}Y_{0.79}$(acac)$_3$phen] complex shows a significant pressure sensitivity on the Tb^{3+}/Eu^{3+} LIR. Dilution by Y^{3+} in the system affects the evolution of Tb^{3+} emission under variation in hydrostatic pressure, so the variation in LIR induced by pressure becomes reversible with dilution by Y^{3+}. The temperature-induced variation in the LIR is verified and can be corrected by temperature calibration for pressure measurement. Therefore, the [Ln(acac)$_3$phen] (Ln^{3+} = Y^{3+}, Tb^{3+}, Eu^{3+}) complex can be a reliable photoluminescent (PL) sensor in pressure-sensing applications in the range 0–700 MPa pressure, marking an important advance in short-range PL pressure sensors.

4 Materials and methods

4.1 Complex synthesis

Commercial chemical reagents and solvents were used without further purification. The [(Ln)(acac)$_3$phen] complexes were prepared based on literature synthesis.[60,62] The alcoholic solution of the 0.2 M mixed Ln(III) was prepared by dissolving hydrated $LnCl_3$ (hydrated YCl_3, 99.9% (Alfa Aesar, Haverhill, MA, USA), hexahydrated $TbCl_3$ 99.9% (Thermo Fisher Scientific, Waltham, MA, USA), hydrated $EuCl_3$ 99.9% (Alfa Aesar)) in methanol at different compositions. Then, the ligand 1,10-phenanthroline (1,10-phenanthroline powder monohydrate, 99+%, Alfa Aesar) was added to the MeOH solution at a concentration of 0.2 M. After the solid compounds had dissolved, acetylacetone (2.4-pentanedion Reagent plus >99%, Sigma-Aldrich Chemie GmbH, Taufkirchen, Germany) was added to the solution at a concentration of 0.6 M with mechanical stirring. The mixture was stirred for 30 min at room temperature and then triethylamine (Et_3N, > 99.5%, Sigma-Aldrich) was added. The solution was then stirred for a further 15 min and stored in the refrigerator at 3–5 °C for subsequent crystallization. After 24–48 h, the formed colorless crystals were separated from the solution and washed with a small amount of EtOH. Attenuated total-reflectance (ATR) infrared (IR) spectra of pure solid samples were recorded on using a SAFRAS FT-IR spectrometer. FTIR (cm^{-1}): ν(C=O) ~ 1620(m); ν(C=C) ~ 1591(m); ν(C=N) ~ 1515.

4.2 Structural characterizations

The crystal structure was defined by an X-ray powder diffractometer (Bruker D8 Advance diffractometer, Bruker, Billerica, MA, USA), equipped with the Cu Kα radiation (λ = 1.54060 Å). Powder XRD diagrams were collected under 45 kV and 30 mA at room temperature. Scanning electron microscopy (SEM) images and elemental EDS spectra of the complex were captured by the Zeiss Merlin Compact (Zeiss, Germany) operating at 20 kV (Centre Technologique des Microstructures de l'Université de Lyon). These EDX measurements strongly support the monophasic character of all the samples.

The [$Eu_{0.01}Tb_{0.2}Y_{0.79}$(acac)$_3$phen] single crystal was selected and mounted on an XtaLAB Synergy, Dualflex, HyPix-Arc 100° diffractometer (Rigaku, Tokyo, Japan). Data collection was achieved at 100.0(3) K using Molybdenum X-ray radiation (λ = 0.71073 Å). Intensities were collected using the CrysalisPro software (Rigaku, Tokyo, Japan).[84] Reflection indexing, unit-cell parameter refinement, Lorentz-polarization correction, peak integration, and background determination were performed with the CrysalisPro software.

The $Eu_{0.01}Tb_{0.2}Y_{0.79}(acac)_3phen]$ structure was solved by direct methods using ShelXT[106] and refined using ShelXL.[107] The structure was refined using full-matrix least squares on F^2 within the Olex2 suite.[108] All non-hydrogen atoms were refined with anisotropic displacement parameters unless specified otherwise. Disordered portions were modeled using refined partial occupancies. Geometric and vibrational restrictions were applied where appropriate to ensure physically reasonable models. With the metallic position within the mononuclear complex, the Tb^{3+} and Y^{3+} ions were fixed at the same crystallographic position and the restrictions on their position as well as their anisotropic displacement parameters were fixed. Their respective occupancies were refined by fixing the sum equal to 1.

4.3 **Optical characterizations**

The photoluminescent properties were analyzed by a modular spectrofluorometer, equipped with a pulsed multi-wavelength laser (EKSPLA NT230, 50 Hz). The laser spot was non-focused to protect the sample from being destroyed under high-power light. The emission spectra were obtained by a CCD detector (Newton^{EM} EMCCD Camera, Andor, Belfast, UK), and the excitation spectra and the lifetime measurements were performed by a PM detector (Photo-multiplicator, Short Focal Length Triple Grating Imaging Spectrographs, TRIAX 320 HORIBA, Kyoto, Japan). The temperature variation was controlled by a thermo-cell (Optical DSC600 cell, LINKAM, Tadworth, UK), supported by liquid nitrogen flux for low temperature (<293 K). Data were collected after 10 s of temperature stabilization.

4.4 **Emission spectra under pressure**

Pressure calibration experiments (≤1 GPa) were performed in a high-pressure DAC: MDAC type BHP for Biology 100° symmetrical aperture, Betsa, Paris, France). The DAC was coupled with a focused continued laser (405 nm) with a micron-scale rounded spot. The laser power was measured in front of the diamond window, at around 0.5 mW. The emission signals were collected and analyzed using a CCD detector (U1000 Horiba Jobin-Yvon Spectrometer, Kyoto, Japan). The mini crystals were dispersed in Squalane ($C_{30}H_{62}$) as a hydrostatic pressure medium. Based on our previous work,[24] the DAC was equipped with a culet diamond anvil (1.4 mm), a thick diamond window (400 mm), and a nickel gasket between them. This elastic gasket allows buffering of the applied pressure, which has about 0.2 mm of thickness, and a 0.5 mm diameter hole in the middle. An internal membrane inflated by N_2 gas covers and closes the DAC to apply pressure. The temperature was regulated by a heating ring (External Heating System, Betsa) around the DAC, the inserted thermocouple was placed next to the metal gasket in the DAC, which allows measurement of the sample temperature with a precision of ±0.1 K. A small volume of suspended sample (<1 µL) was introduced into the gasket hole during measurement, and several ruby microparticles (>3 µm) were introduced with as a tool for internal pressure calibration. The resolution of pressure sensing is estimated to 30 MPa.[109] Data were collected after 20 min to ensure stabilization of pressure and temperature. Based on literature,[10,110] upon 405 nm excitation, the commercial ruby microparticles are used as a reliable pressure sensor by their photoluminescent wavelength shift R_1 (around 694.3 nm at ambient pressure). The spectral wavelength was corrected by a Neon lamp (ORIEL 6032, Oriel Corp., Stratford, CT, USA) with a peak at 703.24 nm.

4.5 **Luminescent intensity ratio (LIR) and relative sensitivity (S_R) calculations**

The LIR of the emission of Tb^{3+} and Eu^{3+} were estimated by the integrated areas of the spectral band to include the overall emitted intensities for each sublevel's transition,[111] calculated in the Simpson's rule MATLAB program. The integrated area ranges were 520–560 nm (Tb emission) and 595–635 nm (Eu emission). The S_R values are estimated by equation S3 below 700 MPa.

ASSOCIATED CONTENT

Supporting information

Equation S1-S3

Figures S1–S12

Table S1–S4

AUTHOR INFORMATION

Corresponding authors

* Laurence Bois

Correspondence: laurence.bois@univ-lyon1.fr

* David Philippon

Correspondence: david.philippon@insa-lyon.fr

Author contributions

C.J., L.B., D.P. and S.D. are the supervisors of projects. Y.Z., L.B., G.L. G.P., M.C. and D.P. performed the experiments. L.B., G.L., D.P., G.P., L.L. and E.J. provided input for the design of the experiments. Y.Z., L.B., G.L., G.P., D.P. and S.D. co-wrote the manuscript with input from other authors.

Funding Sources

This work was supported by the LABEX MANUTECH-SISE (ANR-10-LABX-0075) of Université de Lyon, within the Plan France 2030 operated by the French National Research Agency (ANR).

ACKNOWLEDGMENT

The authors gratefully acknowledge the Ctμ platform of electronic microscopy (University Lyon 1), Ruben Vera in the "Centre de Diffractométrie Henri Longchambon" (University Lyon 1), also Zhou Zhijian for his indispensable help in data processing. The authors sincerely thank all the support from the LABEX MANUTECH-SISE (ANR-10-LABX-0075) of Université de Lyon.

References:

[1] S. M. Borisov, I. Klimant, *Analyst* **2008**, *133*, 1302-1307.

[2] P. Panda, A. Dutta, S. Pal, D. Ganguly, S. Chattopadhyay, N. C. Das, R. K. Das, *New J. Chem* **2023**, *47*, 5734.

[3] R. Gao, X. Fang, D. Yan, *J. Mater. Chem. C* **2019**, *7*, 3399.

[4] Y. Hasegawa, Y. Kitagawa, *J. Mater. Chem. C* **2019**, *7*, 7494.

[5] A. N. Carneiro Neto, E. Mamontova, A. M. P. Botas, C. D. S. Brites, R. A. S. Ferreira, J. Rouquette, Y. Guari, J. Larionova, J. Long, L. D. Carlos, *Adv. Opt. Mater.* **2022**, *10*, 2101870.

[6] Y. Zhou, G. Ledoux, D. Philippon, S. Descartes, M. Martini, S. He, C. Desroches, D. Fournier, C. Journet, L. Bois, *ACS Appl. Nano Mater.* **2022**, *5*, 16388.

[7] E. Homeyer, S. Pailhès, R. Debord, V. Jary, C. Dujardin, G. Ledoux, *Appl. Phys. Lett.* **2015**, *106*, 243502.

[8] C. D. S. Brites, S. Balabhadra, L. D. Carlos, *Adv. Opt. Mater.* **2019**, *7*, 5, 1801239.

[9] D. Parker, P. Kanthi Senanayake, J. A. Gareth Williams, *J. Chem. Soc. Perkin Trans. 2* **1998**, 2129.

[10] H. K. Mao, J. Xu, P. M. Bell, *J. Geophys. Res.* **1986**, *91*, 4673.

[11] M. Pieprz, M. Runowski, K. Ledwa, J. J. Carvajal, A. Bednarkiewicz, L. Marciniak, *ACS Appl. Mater. Interfaces* **2023**, *1*, 1080..

[12] M. Runowski, J. Marciniak, T. Grzyb, D. Przybylska, A. Shyichuk, B. Barszcz, A. Katrusiak, S. Lis, *Nanoscale* **2017**, *9*, 16030.

[13] J. R. Casar, C. A. McLellan, C. Siefe, J. A. Dionne, *ACS Photonics* **2021**, *8*, 3.

[14] A. Lay, O. H. Sheppard, C. Siefe, C. A. Mclellan, R. D. Mehlenbacher, S. Fischer, M. B. Goodman, J. A. Dionne, *ACS Cent. Sci.* **2019**, *5*, 1211.

[15] A. Lay, C. Siefe, S. Fischer, R. D. Mehlenbacher, F. Ke, W. L. Mao, A. P. Alivisatos, M. B. Goodman, J. A. Dionne, *Nano Lett.* **2018**, *18*, 4454.

[16] A. Lay, D. S. Wang, M. D. Wisser, R. D. Mehlenbacher, Y. Lin, M. B. Goodman, W. L. Mao, J. A. Dionne, *Nano Lett.* **2017**, *17*, 4172.

[17] M. Runowski, A. Shyichuk, A. Tymiński, T. Grzyb, V. Lavín, S. Lis, *ACS Appl. Mater. Interfaces* **2018**, *10*, 17269.

[18] C. A. McLellan, C. Siefe, J. R. Casar, C. S. Peng, S. Fischer, A. Lay, A. Parakh, F. Ke, X. W. Gu, W. Mao, S. Chu, M. B. Goodman, J. A. Dionne, *J. Phys. Chem. Lett.* **2022**, *13*, 1547.

[19] E. Vorathin, Z. M. Hafizi, N. Ismail, M. Loman, *Opt. Laser Technol.* **2020**, *121*, 105841..

[20] M. Runowski, P. Woźny, I. R. Martín-Benenzuela, *J. Mater. Chem. C* **2021**, *9*, 4643..

[21] M. Runowski, T. Zheng, P. Woźny, P. Du, *Dalt. Trans.* **2021**, *50*, 14864.

[22] N. Stopikowska, Q. Guo, S. Lis, M. Runowski, *ACS Appl. Mater. Interfaces* **2019**, *11*, 4131.

[23] R. D. Mehlenbacher, R. Kolbl, A. Lay, J. A. Dionne, *Nat. Rev. Mater.* **2017**, *3*, 1.

[24] T. Seoudi, D. Philippon, N. Fillot, L. Lafarge, N. Devaux, A. Mondelin, P. Vergne, *Tribol. Lett.* **2020**, *68*, 3, 1..

[25] S. M. B. Albahrani, T. Seoudi, D. Philippon, L. Lafarge, P. Reiss, H. Hajjaji, G. Guillot, M. Querry, J. M. Bluet, P. Vergne, *RSC Adv.* **2018**, *8*, 22897.

[26] Y. Wang, T. Seto, K. Ishigaki, Y. Uwatoko, G. Xiao, B. Zou, G. Li, Z. Tang, Z. Li, Y. Wang, *Adv. Funct. Mater.* **2020**, *30*, 1.

[27] A. V. M. De Andrade, R. L. Longo, A. M. Simas, G. F. De Sá, *J. Chem. Soc. - Faraday Trans.* **1996**, *92*, 1835.

[28] M. Kleinerman, *J. Chem. Phys.* **1969**, *51*, 2370.

[29] P. Yuster, S. I. Weissman, *J. Chem. Phys.* **1949**, *17*, 1182.

[30] S. I. Weissman, *J. Chem. Phys.* **1942**, *10*, 214.

[31] P. A. Tanner, W. Thor, Y. Zhang, K. L. Wong, *J. Phys. Chem. A* **2022**, *126*, 7418.

[32] T. Zahariev, D. Shandurkov, S. Gutzov, N. Trendafilova, D. Enseling, T. Jüstel, I. Georgieva, *Dye. Pigment.* **2021**, *185*, 108890.

[33] K. Binnemans, *Chem. Rev.* **2009**, *109*, 4283.

[34] J.-C. G. Bünzli, S. V. Eliseeva, *Lanthanide Luminescence*, *Photophysical, Analytical and Biological Aspects*, Editors P. Hänninen, H. Härmä, Springer Science, **2010**.

[35] K. A. Romanova, A. Y. Freidzon, A. A. Bagaturyants, Y. G. Galyametdinov, *J. Phys. Chem. A* **2014**, *118*, 11244.

[36] J. C. G. Bünzli, C. Piguet, *Chem. Soc. Rev.* **2005**, *34*, 1048.

[37] Y. Kitagawa, P. P. Ferreira Da Rosa, Y. Hasegawa, *Dalt. Trans.* **2021**, *50*, 14978.

[38] Y. Kitagawa, M. Kumagai, T. Nakanishi, K. Fushimi, Y. Hasegawa, *Inorg. Chem.* **2020**, *59*, 5865.

[39] M. Yamamoto, Y. Kitagawa, T. Nakanishi, K. Fushimi, Y. Hasegawa, *Chem. - A Eur. J.* **2018**, *24*, 17719.

[40] W. P. Lustig, J. Li, *Coord. Chem. Rev.* **2018**, *373*, 116.

[41] T. Förster, *Ann. Phys.* **1948**, *6*, 55.

[42] D. L. Dexter, *J. Chem. Phys.* **1953**, *21*, 836.

[43] D. L. Dexter, J. H. Schulman, *J. Chem. Phys.* **1954**, *22*, 1063.

[44] T. Förster, *Discuss. Faraday Soc.* **1959**, *27*, 7.

[45] S. Speiser, *Chem. Rev.* **1996**, *96*, 1953.

[46] S. Goderski, M. Runowski, P. Woźny, V. Lavín, S. Lis, *ACS Appl. Mater. Interfaces* **2020**, *12*, 40475.

[47] T. Zheng, M. Runowski, J. Xue, L. Luo, U. R. Rodríguez-Mendoza, V. Lavín, I. R. Martín, P. Rodríguez-Hernández, A. Muñoz, P. Du, *Adv. Funct. Mater.* **2023**, 33, *2214663*.

[48] T. Zheng, M. Runowski, P. Rodríguez-Hernández, A. Muñoz, F. J. Manjón, M. Sójka, M. Suta, E. Zych, S. Lis, V. Lavín, *Acta Mater.* **2022**, *231*, 117886.

[49] T. Zheng, M. Runowski, P. Woźny, S. Lis, V. Lavín, *J. Mater. Chem. C* **2020**, *8*, 4810.

[50] M. Runowski, P. Woźny, N. Stopikowska, Q. Guo, S. Lis, *ACS Appl. Mater. Interfaces* **2019**, *11*,

4131.

[51] M. A. Antoniak, S. J. Zelewski, R. Oliva, A. Żak, R. Kudrawiec, M. Nyk, *ACS Appl. Nano Mater.* **2020**, *3*, 4209.

[52] M. Szymczak, M.Runowski, M. G. Brik, L. Marciniak, *Chem. Eng. J.* **2023**, *466*, 143130.

[53] T. Zheng, M. Runowski, I. R. Martín, K. Soler-Carracedo, L. Peng, M. Skwierczyńska, M. Sójka, J. Barzowska, S. Mahlik, H. Hemmerich, F. Rivera-López, P. Kulpiński, V. Lavín, D. Alonso, D. Peng, *Adv. Mater.* **2023**, *35*, 2304140..

[54] M. Runowski, P. Woźny, S. Lis, V. Lavín, I. R. Martín, *Adv. Mater. Technol.* **2020**, *5*, 1.

[55] C. Hernandez, S. K. Gupta, J. P. Zuniga, J. Vidal, R. Galvan, H. Guzman, L. Chavez, K. Lozano, Y. Mao, *J. Mater. Sci. Technol.* **2021**, *66*, 103.

[56] H. Y. Wong, X. Le Zhou, C. T. Yeung, W. L. Man, P. Woźny, A. Półrolniczak, A. Katrusiak, M. Runowski, G. L. Law, *Chem. Eng. J. Adv.* **2022**, *11*, 100326.

[57] F. Piccinelli, C. De Rosa, A. Lazarowska, S. Mahlik, M. Grinberg, T. Nakanishi, S. Omagari, M. Bettinelli, *Inorganica Chim. Acta* **2020**, *499*, 119179.

[58] Y. Amao, I. Okura, T. Miyashita, *Bull. Chem. Soc. Jpn.* **2000**, *73*, 2663.

[59] M. Kasai, Y. Sugioka, M. Yamamoto, T. Nagata, T. Nonomura, K. Asia, Y. Hasegawa, *Sensors* **2020**, *20*, 1.

[60] S. Petit, F. Baril-Robert, G. Pilet, C. Reber, D. Luneau, *J. Chem. Soc. Dalt. Trans.* **2009**, *34*, 6809.

[61] R. C. Knighton, L. K. Soro, A. Lecointre, G. Pilet, A. Fateeva, L. Pontille, L. Francés-Soriano, N. Hildebrandt, L. J. Charbonnière, *Chem. Commun.* **2021**, *57*, 53.

[62] F. Baril-Robert, S. Petit, G. Pilet, G. Chastanet, C. Reber, D. Luneau, *Inorg. Chem.* **2010**, *49*, 10970.

[63] K. Nehra, A. Dalal, A. Hooda, S. Singh, D. Singh, S. Kumar, R. Singh, R. Kumar, P. Kumar, *Inorganica Chim. Acta* **2022**, *539*, 121007.

[64] Z. Yu, L. Shen, D. Li, E. Yue, B. Pun, X. Zhao, H. Lin, *Sci. Rep.* **2020**, *10*, 926.

[65] L. Lin, Z. Li, Z. Wang, Z. Feng, F. Huang, Q. Dai, Z. Zheng, *Opt. Mater. (Amst).* **2020**, *110*, 110532.

[66] R. Ilmi, S. Kansız, N. Dege, M. S. Khan, *J. Photochem. Photobiol. A Chem.* **2019**, *377*, 268.

[67] B. V. Bukvetskii, A. G. Mirochnik, A. S. Shishov, *J. Lumin.* **2018**, *195*, 44.

[68] R. Maouche, S. Belaid, B. Benmerad, C. Daiguebonne, Y. Su, K. Bernot, O. Guillou, *Inorg. Chem.* **2021**, *60*, 3707.

[69] A. V Shurygin, V. I. Vovna, V. V Korochentsev, A. G. Mirochnik, I. V Kalinovskaya, V. I. Sergienko, *Spectrochim. Acta Part A Mol. Biomol. Spectrosc.* **2019**, *213*, 176.

[70] A. G. Mirochnik, B. V Bukvetskii, P. A. Zhikhareva, V. E. Karasev, *Russ. J. Coord. Chem.* **2001**, *27*, 475.

[71] T. Zahariev, N. Trendafilova, I. Georgieva, *Mater. Today Proc.* **2022**, *61*, 1292.

[72] O. T. Alexander, R. E. Kroon, A. Brink, H. G. Visser, *Dalt. Trans.* **2019**, *48*, 16074.

[73] J. Kido, W. Ikeda, M. Kimura, K. Nagai, *Japanese J. Appl. Physics, Part 2 Lett.* **1996**, *35*, L394.

[74] J. Kido, Y. Okamoto, *Chem. Rev.* **2002**, *102*, 2357.

[75] W. L. Li, Z. Q. Gao, Z. Y. Hong, C. S. Lee, S. T. Lee, *Synth. Met.* **2000**, *111*, 53.

[76] A. Edgar, *Luminescent Materials* . In: Kasap, S., Capper, P. (eds) Springer Handbook of Electronic and Photonic Materials. Springer Handbooks. Springer, Boston, MA. **2006**

[77] A. N. Carneiro Neto, R. T. Moura, A. Shyichuk, V. Paterlini, F. Piccinelli, M. Bettinelli, O. L. Malta, *J. Phys. Chem. C* **2020**, *124*, 10105.

[78] F. Baur, F. Glocker, T. Jüstel, *J. Mater. Chem. C* **2015**, *3*, 2054.

[79] V. E. Gontcharenko, M. A. Kiskin, V. D. Dolzhenko, V. M. Korshunov, I. V Taydakov, Y. A. Belousov, *Molecules* **2021**, *26*, 1.

[80] C. Blais, C. Daiguebonne, Y. Suffren, K. Bernot, G. Calvez, L. Le Pollès, C. Roiland, S. Freslon, O. Guillou, *Inorg. Chem.* **2022**, *61*, 11897.

[81] M. Kato, K. Ishii, *Soft Crystals*. Toward the Applications of Soft Crystals. In: Kato, M., Ishii, K. (eds) Soft Crystals. The Materials Research Society Series. Springer, Singapore. **2023**

[82] W. H. Watson, R. J. Williams, N. R. Stemple, *J. Inorg. Nucl. Chem.* **1972**, *34*, 501.

[83] S. Ogata, A. Ishii, C. L. Lu, T. Kondo, N. Yajima, M. Hasegawa, *J. Photochem. Photobiol. A Chem.* **2017**, *334*, 55.

[84] Rigaku Oxford Diffraction, *Rigaku Corp. Wroclaw, Pol.* **2022**.

[85] Y. M. Fadieiev, S. S. Smola, E. V. Malinka, N. V. Rusakova, *J. Lumin.* **2017**, *183*, 121.

[86] Y. Kitagawa, M. Tsurui, Y. Hasegawa, *RSC Adv.* **2022**, *12*, 810.

[87] G. Bao, K. L. Wong, D. Jin, P. A. Tanner, *Light Sci. Appl.* **2018**, *7*, 96.

[88] Y. Hasegawa, Y. Kitagawa, T. Nakanishi, *NPG Asia Mater.* **2018**, *10*, 52.

[89] X. W. Peng, Q. Y. Liu, H. H. Wang, Y. L. Wang, *Dye. Pigment.* **2019**, *162*, 405.

[90] J. Kai, M. C. F. C. Felinto, L. A. O. Nunes, O. L. Malta, H. F. Brito, *J. Mater. Chem.* **2011**, *21*, 3796.

[91] L. Wu, Y. Fang, W. Zuo, J. Wang, J. Wang, S. Wang, Z. Cui, W. Fang, H. L. Sun, Y. Li, X. Chen, *JACS Au* **2022**, *2*, 853.

[92] F. S. de Vicente, P. Freddi, A. J. G. Otuka, C. R. Mendonça, H. F. Brito, L. A. O. Nunes, D. R. Vollet, D. A. Donatti, *J. Lumin.* **2018**, *197*, 370.

[93] R. M. Ranson, E. Evangelou, C. B. Thomas, *Appl. Phys. Lett.* **1998**, *72*, 2663.

[94] M. D. Chambers, D. R. Clarke, *Annu. Rev. Mater. Res.* **2009**, *39*, 325.

[95] M. L. Debasu, D. Ananias, A. G. Macedo, J. Rocha, L. D. Carlos, *J. Phys. Chem. C* **2011**, *115*, 15297.

[96] ManjuBala, S. Kumar, S. Chahar, V. B. Taxak, P. Boora, S. P. Khatkar, *Optik (Stuttg).* **2020**, *202*,

163636.

[97] S. Omagari, T. Nakanishi, Y. Kitagawa, T. Seki, K. Fushimi, H. Ito, A. Meijerink, Y. Hasegawa, *Sci. Rep.* **2016**, *6*, 1.

[98] S. S. Dudar, E. B. Sveshnikova, A. V Shablya, V. L. Ermolaev, *High energy Chem.* **2007**, *41*, 189.

[99] C. Piguet, A. F. Williams, G. Bernardinelli, E. Moret, J. G. Bünzli, *Helv. Chim. Acta* **1992**, *75*, 1697.

[100] M. Szymczak, P. Woźny, M. Runowski, M. Pieprz, V. Lavín, L. Marciniak, *Chem. Eng. J.* **2023**, *453*, 1.

[101] M. Szymczak, M. Runowski, V. Lavín, L. Marciniak, *Laser Photonics Rev.* **2023**, *17*, 2200801.

[102] R. Marin, N. C. Millan, L. Kelly, N. Liu, E. M. Rodrigues, M. Murugesu, E. Hemmer, *J. Mater. Chem. C* **2022**, *10*, 1767.

[103] V. Trannoy, A. N. Carneiro Neto, C. D. S. Brites, L. D. Carlos, H. Serier-Brault, *Adv. Opt. Mater.* **2021**, *9*, 2001938.

[104] S. A. Wade, S. F. Collins, G. W. Baxter, *J. Appl. Phys.* **2003**, *94*, 4743.

[105] C. D. S. Brites, A. Millán, L. D. Carlos, Chapter 281- *Lanthanides in Luminescent Thermometry*, B. Jean-Claude, P. Vitalij K (Eds.), Handbook on the Physics and Chemistry of Rare Earths, Elsevier, 339-427, **2016**.

[106] G. M. Sheldrick, *Acta Crystallogr. Sect. A Found. Crystallogr.* **2015**, *71*, 3.

[107] G. M. Sheldrick, *Acta Crystallogr. Sect. C Struct. Chem.* **2015**, *27*, 3.

[108] O. V. Dolomanov, L. J. Bourhis, R. J. Gildea, J. A. K. Howard, H. Puschmann, *J. Appl. Crystallogr.* **2009**, *42*, 339.

[109] A. Picard, P. M. Oger, I. Daniel, H. Cardon, G. Montagnac, J. C. Chervin, *J. Appl. Phys.* **2006**, *100*, 034915.

[110] O. Grasset, *High Press. Res.* **2001**, *21*, 139.

[111] N. Rakov, G. S. Maciel, M. Xiao, *Electron. Mater. Lett.* **2014**, *10*, 985.

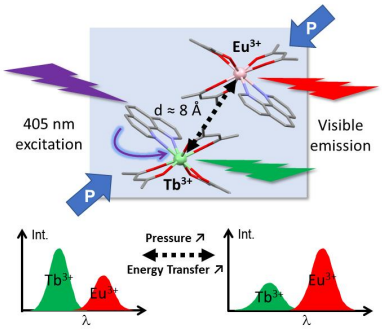

A highly sensitive reversible pressure sensor designed for short-range applications (below 700 MPa) is demonstrated, using a luminescent mixed lanthanide complex. This mononuclear complex, containing terbium, europium and yttrium enables pressure-sensitive Tb^{3+}/Eu^{3+} energy transfer with reversibility. As pressure increases, the relative intensity of Tb^{3+}/Eu^{3+} emission decreases, leading to exceptional pressure sensitivity based on luminescence intensity ratios.